Int J Adv Manuf Technol (2017) 92:3273–3286
DOI 10.1007/s00170-017-0385-z

ORIGINAL ARTICLE

Study on the surface topography considering grinding chatter based on dynamics and reliability

Cong Sun [1] · **Yijing Niu** [1] · **Zhenxin Liu** [1] · **Yushi Wang** [1] · **Shichao Xiu** [1]

Received: 10 January 2017 / Accepted: 3 April 2017 / Published online: 21 April 2017

Abstract Surface grinding is always accompanied with chatter due to self-excited vibration. It often leads to an unexpected impact on the quality of the workpiece's topography. However, the chatter is regarded as a harmonic vibration in most topography researches. This may lose preciseness when the relative vibration and the abrasive trajectory are taken into consideration. In order to study the relationship between the system's dynamic characteristic and the workpiece's topography, a two-DOF (degree of freedom) dynamic model with time-delay characteristic is established accordingly. Then, reliability analysis is introduced into chatter vibration by analyzing the fluctuations of dynamic parameters with two analysis methods, namely Monte Carlo (MC) and first-order second-moment (FOSM). With the above two reliability analysis methods, the calculations are carried out as follows: firstly, the non-Gaussian distribution of the grinding wheel based on Johnson Curves and filter techniques is established. Secondly, the results of the dynamic analysis are coupled into the grain trajectory equation. Thirdly, the influence of the wheel grinding parameters and dynamic parameters on the surface height is discussed by coupling the dynamic characteristics into the simulation model. Finally, the simulations and experiments are carried out on the impact of different feeding rates and sections on the workpiece to the surface heights. The comparisons verify the prediction of the simulation model. The obtained conclusions could be applied to optimize the workpiece's topography by regulating the grinding parameters and dynamic parameters to weaken the chatter's influence.

Keywords Surface grinding · Grinding chatter · Workpiece's topography · Reliability analysis · Dynamic characteristic · Grain trajectory · Surface height

1 Introduction

Surface grinding is widely applied in high-precision machining with low material-removal rate and high surface precision. The surface topography is the response of the interaction between the wheel's abrasive grains and the workpiece surface's material [1–6]. In addition, the change of surface topography affects the stress distribution, waviness, and contact fatigue limit directly [7]. Various factors have influence on the surface topography, especially the relative movement between the abrasive grains and the workpiece [8]. The relative movement is decided by the system's dynamics. It was verified that the wheel's dynamics and the surface topography are closely related [9]. Therefore, it is necessary to make a dynamic analysis on the system. The output of the dynamic response is the vibration. There are two kinds of vibration forms including the grinding chatter and the forced vibration. The forced vibration is commonly seen in the cylindrical grinding. Due to the deficiency of the process system's rigidity which leads to the deformation of the workpiece, the vibration becomes stronger. However, the forced vibration may not be suitable for the surface grinding, because the workpiece's fixture is of great rigidity. Therefore, the forced vibration is neglected in the regular surface grinding. As is known, the source of the surface grinding vibration belongs to the regenerative chatter,

✉ Shichao Xiu
a20082051@163.com

[1] School of Mechanical Engineering and Automation, Northeastern University, Heping Region Wenhua Road, Shenyang 110819, China

which is produced from the metal cutting operations such as grinding, milling, drilling, etc. [10]. The regenerative chatter with time-delay characteristic is a kind of self-excited vibration caused by the phase difference from the two adjacent grains [11, 12]. The regenerative chatter and the randomly distributed abrasive grains make the grinding process complicated. However, the chatter is always neglected when it comes to the surface topography. Even though the vibration is considered, the mode of vibration is still regarded as a kind of forced vibration. Therefore, solving the dynamic equations and analyzing the fluctuations of dynamic parameters within the machining error range are of great significance in improving the quality of surface topography.

The surface topography is affected by the grinding chatter. Chatter stems from the unbalance of the grinding system [13]. Therefore, the unbalance of the grinding wheel is analyzed by the lobe diagram [14–16]. For the reason that it can be a reference standard to measure the chatter's strength, the contact stiffness between the wheel and the workpiece is discussed, which is an important affecting parameter of the lobe diagram. Since the contact stiffness is affected by the dynamic parameters, the study on dynamic parameters is carried out. The reason why the grinding dynamic parameters are not always the same as the set values under the actual working conditions is that the dynamic parameters fluctuate in a short range which is caused by interference and the machining errors. Therefore, the reliability for random factors analysis is introduced with two methods. Monte Carlo (MC) is applied to settle the influence of the dynamic parameters' fluctuation, and the first-order second-moment method (FOSM) is used to verify the accuracy of MC [17, 18]. Then, the dynamic characteristic of the system chatter is coupled into the analysis of workpiece's surface topography.

For the sake of studying the relationship between the dynamic characteristics of system chatter and the workpiece's surface topography, the model of the grinding surface should be established first. Zhou and Xi created a truncated Gaussian distribution model to relate the wheel volume wear to the change of protrusion's heights [19]. Yan and Rong established the mathematical model of the abrasive grains based on the Gaussian distribution [20]. Xie and Williams made a prediction on a hard rough surface on the assumption that the grains' heights were regarded as Gaussian distribution [21]. To sum up, all the simulated models above are based on the Gaussian distribution. However, the wheel's surface always shows a negative skewness to some extent. When the wheel's machining process is considered, the peak of the rough surface is easier to be removed than the valley. Therefore, it is believed that the height of the abrasive grains seemingly belongs to non-Gaussian distribution [22, 23]. The non-Gaussian distribution of the wheel and the system's dynamic interactions result in the complexity of workpiece's surface topography. Yang and Guo analyzed the effect of the vibration on the assumption that the wheel's surface was treated to be smooth [24]. Cao and Wang simulated workpiece's surface topography when the wheel's and workpiece's vibrations were taken into account. However, the vibrations were regarded as a type of fixed amplitude harmonic vibration [1, 7]. To sum up, the majority of the existed vibration researches are based on the simple vibration form. When the chatter happens, the vibration style and the vibration amplitude are time-varying and should be reconsidered.

After confirming the chatter's dynamic characteristic and the surface topography of the grinding wheel, a new simulation model for workpiece's surface is established. The stability and reliability of the system are analyzed firstly, and then the system's dynamic solution and parameter fluctuations are coupled into the interactions between the abrasive grains and the wheel's surface. Based on the new method, the simulation is in the same order of magnitude with the result of experiments. It shows that chatter can directly increase the values of the workpiece's surface height. The fluctuations of the grinding system's dynamic parameters will lead to differences in chatter's stability and reliability. As a consequence, the abrasive grains trajectory on the workpiece is influenced. Finally, the workpiece's surface is affected accordingly. Therefore, the chatter factors should be seriously taken into consideration when it comes to the analysis of the workpiece's surface topography.

2 Analysis of the grinding system

2.1 Dynamic modeling

In order to study the dynamic characteristic of the grinding system, a two-DOF (degree of freedom) dynamic model in the normal direction is established in Fig. 1. The wheel (mass M_g) rotates at the angular velocity of ω, and the workpiece's (mass M_w) material is 1045 steel, which begins with the feeding rate of v_w. The normal cutting force F_N between the wheel and the workpiece is considered to be nonlinear due to the chatter factors. The equations of the entire two-DOF dynamic system are as follows:

$$M_g\ddot{x}_g + C_g x_g + K_g x_g = F_N \tag{1}$$

$$M_w\ddot{x}_w + C_w x_w + K_w x_w = -F_N \tag{2}$$

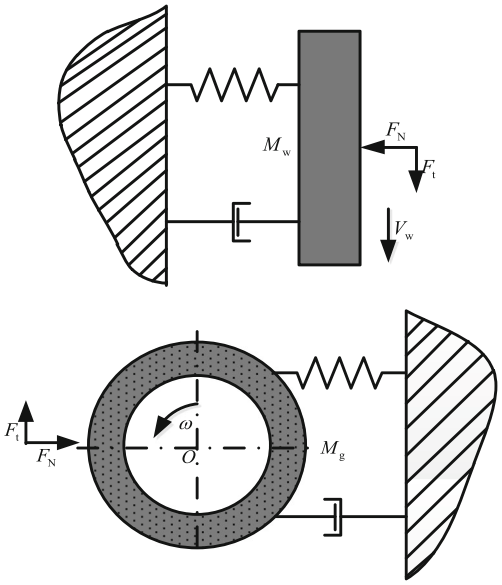

Fig. 1 The surface grinding model

Where C_g, C_w, K_g, K_w, x_g, and x_w are the damping coefficients, the stiffness and the displacement of the wheel and workpiece respectively. The normal cutting force F_N at the grinding position is given by [25]

$$F_N = K_n\Big((1-\alpha)\varepsilon_0 + (1-\alpha\gamma)\big(x_w(t)-x_g(t)\big) - (1-\gamma)\big(x_w\big(t-T_g\big)-x_g\big(t-T_g\big)\big)\Big) \tag{3}$$

Where K_n is the contact stiffness between the workpiece and the wheel. T_g is the time delay of the grinding system and it is also the rotation period of the wheel. ε_0 is the pre-set grinding depth. γ is the cutting ratio of the grinding system. The value of γ ranges from 2×10^{-4} to 1. When γ is relatively smaller, the wheel should get harder. As a result, the grinding force increases. Or else, the grinding force decreases with the increase of γ; meanwhile, the wheel is easy to be worn out. α is the overlapping factor which is related to the contact arc length L_s, the workpiece feeding rate v_w, and the time delay T_g, and it can be written as:

$$\alpha = 1-\frac{2\pi v_w}{L_s\omega_g} \tag{4}$$

Where the contact arc length can be written as $L_s = \sqrt{\varepsilon_0 d_s}$. d_s is the wheel diameter. Furthermore, ε_0 is the grinding depth related to the entire penetration. The entire penetration can be written as (see Fig. 2):

$$\varepsilon(t) = \varepsilon_g(t) + \varepsilon_w(t) = \varepsilon_0 + \Delta\varepsilon(t) \tag{5}$$

Where $\Delta\varepsilon(t)$ is the time-varying part of the entire penetration. $\varepsilon_g(t)$ and $\varepsilon_w(t)$ are penetrations from the wheel and workpiece surface respectively, which can be defined as:

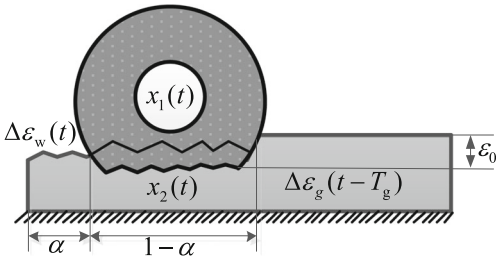

Fig. 2 The grinding contact region

$$\Delta\varepsilon(t) = x_w(t)-x_g(t) \tag{6}$$

$$\varepsilon_g(t) = (1-\gamma)\varepsilon(t) = (1-\gamma)\varepsilon_0 + \Delta\varepsilon_g(t) \tag{7}$$

$$\varepsilon_w(t) = \gamma\varepsilon(t) = \gamma\varepsilon_0 + \Delta\varepsilon_w(t) \tag{8}$$

Where $\Delta\varepsilon_g(t)$ and $\Delta\varepsilon_w(t)$ are the time-varying parts of the $\varepsilon_g(t)$ and the $\Delta\varepsilon_w(t)$. They are related to the calculation of the grinding system, and they can result in the diversity of the workpiece's surface topography with the change of vibrations. Therefore, it is necessary to couple the macro chatter into the microanalysis of the workpiece's surface topography.

In order to solve the delay differential equations, the Runge-Kutta method is adopted in simulation. Vector $\mathbf{y}(t)$ is defined as $\mathbf{y}(t) = \big(x_g(t), x_w(t), x_g(t), x_w(t)\big)^T$. When the

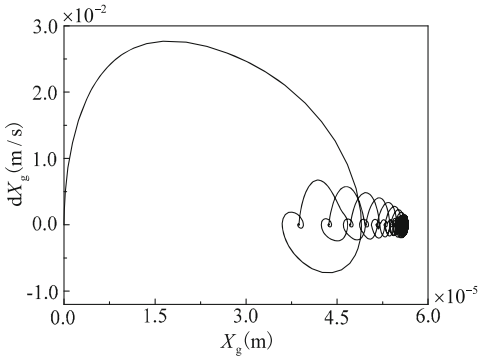

(a)

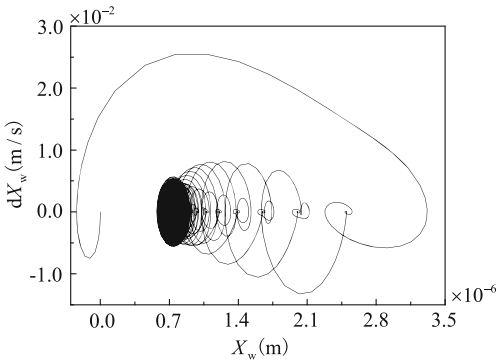

(b)

Fig. 3 The phase-plane diagrams of the grinding system

derivative of $\mathbf{y}(t)$ is calculated, it comes to $\mathbf{y}(t) = \left(x_g(t), x_w(t), \dot{x}_g(t), \dot{x}_w(t)\right)^T$. Finally, the delay differential equations can be written as:

$$\mathbf{y} = \mathbf{M}\mathbf{y} + \mathbf{N}\mathbf{y}\left(t - T_g\right) + \Delta\mathbf{y} \tag{9}$$

Where

$$M = \begin{pmatrix} 0 & 0 & 1 & 0 \\ 0 & 0 & 0 & 1 \\ \dfrac{-K_g - K_n(1-\alpha\gamma)}{M_g} & \dfrac{K_n(1-\alpha\gamma)}{M_g} & -\dfrac{C_g}{M_g} & 0 \\ \dfrac{K_n(1-\alpha\gamma)}{M_w} & \dfrac{-K_w - K_n(1-\alpha\gamma)}{M_w} & 0 & -\dfrac{C_w}{M_w} \end{pmatrix}$$

$$N = \begin{pmatrix} 0 & 0 & 0 & 0 \\ 0 & 0 & 0 & 0 \\ \dfrac{(1-\gamma)K_n}{M_g} & \dfrac{(\gamma-1)K_n}{M_g} & 0 & 0 \\ \dfrac{(\gamma-1)K_n}{M_w} & \dfrac{(1-\gamma)K_n}{M_w} & 0 & 0 \end{pmatrix} \Delta\mathbf{y} = \begin{pmatrix} 0 \\ 0 \\ \dfrac{K_n(1-\alpha)\varepsilon_0}{M_g} \\ \dfrac{K_n(\alpha-1)\varepsilon_0}{M_w} \end{pmatrix}$$

2.2 Response analysis

The phase-plane diagrams of the wheel and the workpiece's stable vibration are shown in Fig. 3. It shows that the chatter amplitude becomes larger at the beginning of grinding. However, as the grinding process continues, the chatter amplitude gets smaller. It is also shown that the wheel's chatter amplitude is much larger than the workpiece's chatter amplitude. Therefore, the wheel's chatter plays a more important role in deciding the stability and reliability of the grinding system.

A key parameter that measures the chatter's strength is the contact stiffness between the wheel and the workpiece. There are many factors contributing to the value of contact stiffness, especially the change of the dynamic parameters. Figure 4 panels a and b are the wheel's dynamic responses under different contact stiffness. The contact stiffness of panel a is 3×10^7 N/m, while the contact stiffness of panel b is 7×10^7 N/m. Panel c is the change of amplitude under different contact stiffness. It can be seen that with the increase of the contact stiffness, the stable chatter becomes unstable gradually and the amplitude increases exponentially.

3 Modeling of the grinding system chatter reliability

3.1 Stability of the grinding chatter

Chatter affects the workpiece's precision and the grinding efficiency to a great extent. When a set of dynamic parameters are given, the contact stiffness can be calculated. Compared with the machine tool with a good rigidity, which is used to fix the workpiece, the wheel's response plays a more important role in deciding the dynamic characteristic. Consequently, as the dynamic approximation, the wheel's responses can replace all DOF. Laplace transformation is applied to Eq. (1):

$$G(s) = \frac{X(s)}{F(s)} = \frac{\dfrac{1}{K_g}}{\left(\frac{s}{\omega_n}\right)^2 + \dfrac{2\xi s}{\omega_n} + 1} \tag{10}$$

Then Laplace transformation is applied to the grinding force F_N, and F_N can be written as:

$$F(i\omega) = K_n\left(A + B\mathrm{e}^{-T_g i\omega}\right)X(i\omega) \tag{11}$$

When Eq. (10) is combined with Eq. (11), it can be obtained that:

$$\frac{1}{-\lambda^2 + 2\xi\lambda i + 1} = \frac{K_g}{K_n(A + B\mathrm{e}^{-T_g\omega i})} \tag{12}$$

Where ξ and ω_n are the damping ratio and nature wheel's frequency respectively. ω is the chatter system's frequency. $A = \alpha\gamma - 1$, $B = 1 - \gamma$. Where $\lambda = \frac{\omega}{\omega_n}$, $\mathrm{e}^{-T_g\omega i} = \cos\left(\omega_g T\right) - i\sin\left(\omega_g T\right)$, Eq. (12) can be expressed as:

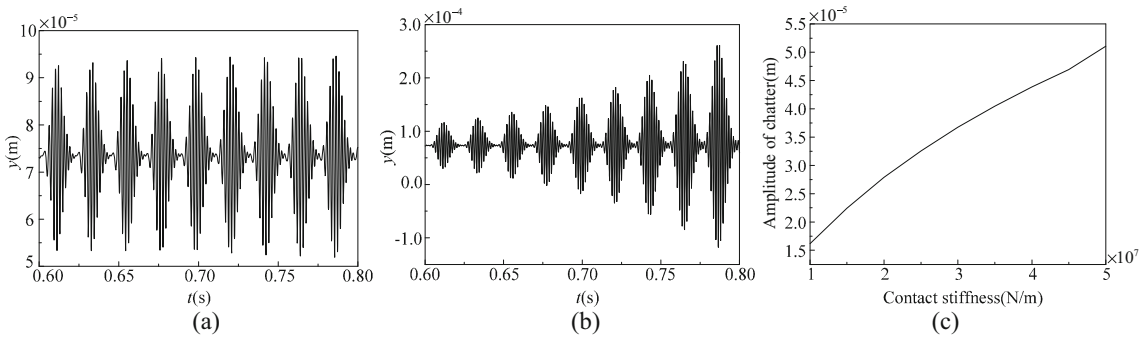

Fig. 4 The response regularity under different contact stiffness

$$\frac{\frac{1-\lambda^2-2\xi\lambda i}{\left(1-\lambda^2\right)^2+(2\xi\lambda)^2}}{=\frac{K_g}{K_n}\cdot\frac{A+B\cos\left(\omega T_g\right)+iB\sin\left(\omega T_g\right)}{\left(A+B\cos\left(\omega T_g\right)\right)^2+B^2\sin^2\left(\omega T_g\right)}} \tag{13}$$

By separating the real and imaginary parts in Eq. (13), it can be obtained that:

$$\frac{\frac{1}{\sqrt{\left(1-\lambda^2\right)^2+(2\xi\lambda)^2}}}{=\frac{K_g}{K_n}\cdot\frac{1}{\sqrt{\left(A+B\cos\left(\omega T_g\right)\right)^2+B^2\sin^2\left(\omega T_g\right)}}} \tag{14}$$

$$\arctan\left(\frac{-2\xi\lambda}{1-\lambda^2}\right)=\arctan\left(\frac{B\sin\left(\omega T_g\right)}{A+B\cos\left(\omega T_g\right)}\right) \tag{15}$$

Where K_n and ωT_g can be written as:

$$K_n=\frac{K_g\sqrt{\left(1-\lambda^2\right)^2+(2\xi\lambda)^2}}{\sqrt{\left(A+B\cos\left(\omega T_g\right)\right)^2+B^2\sin^2\left(\omega T_g\right)}}=\frac{2\xi\lambda K_g}{B\sin\left(\omega T_g\right)} \tag{16}$$

$$\omega T_g=\arcsin\left(\frac{A}{B}\cdot\frac{2\xi\lambda}{\sqrt{\left(\lambda^2-1\right)^2+(2\xi\lambda)^2}}\right)-\arctan\left(\frac{2\xi\lambda}{-\lambda^2+1}\right)+2i\pi\ (i=1,2,3\cdots n) \tag{17}$$

Due to $\omega_n=\frac{2\pi N_g}{60}$ and $T_g=\frac{2\pi}{\omega_n}$, it can be obtained that:

$$N_g=\frac{60\lambda\omega_n}{\omega T_g} \tag{18}$$

When Eq. (17) is combined with Eq. (18), it can be obtained from our operation that:

$$N_g=60\lambda\omega_n\left(\begin{array}{l}\arcsin\left(-\frac{A}{B}\cdot\frac{2\xi\lambda}{\sqrt{\left(\lambda^2-1\right)^2+(2\xi\lambda)^2}}\right)\\-\arctan\left(\frac{2\xi\lambda}{-\lambda^2+1}\right)+2i\pi\end{array}\right)^{-1} \tag{19}$$

According to Eq. (16) and Eq. (19), the lobe diagram about the contact stiffness and the wheel rotation speed under different M_g, C_g, and K_g are shown in Fig. 5

Figure 5 shows the relationship between the wheel rotation speed and the contact stiffness under different mass, stiffness, and damp. It can be seen that contact stiffness fluctuation range becomes larger with the increase of the wheel rotation speed, and the contact stiffness becomes larger with the increase of damp and stiffness, but the increase of mass can result in the decrease of the contact stiffness. It is because that the formula of the contact stiffness is related to M_g, C_g, and K_g as well as the wheel rotation speed. However, when the contact stiffness becomes larger, the grinding force of generating unit displacement gets larger. Therefore, the grinding force acts on the workpiece's surface directly and may have a negative effect on the workpiece's surface.

3.2 Reliability analysis on fluctuated parameters

From Eq. (16), the theoretical parameters are used to be known as fixed parameters such as M_g, K_g, C_g, and chatter frequency ω. However, these parameters are not constant when the machining errors in actual working conditions are taken into consideration. Therefore, the fluctuation of dynamic parameters leads to the uncertainty in the process of grinding. Furthermore, the uncertainty effect can act on the workpiece's surface directly, which may change the scheduled workpiece's surface. In order to study the influence of this uncertainty, reliability analysis is proposed. The reliability is a scale to measure the uncertainty and is a structural reliability of the grinding system. It originates from the fluctuations of

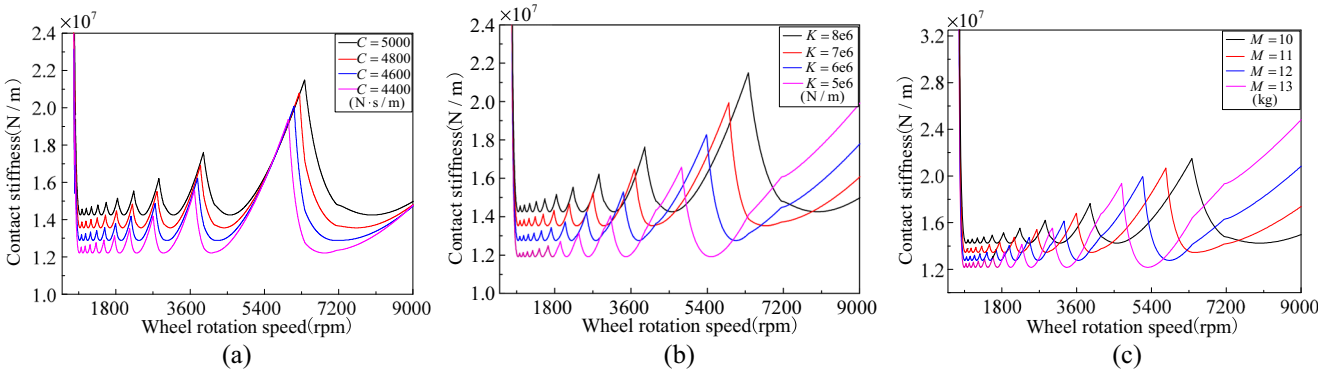

Fig. 5 Typical lobe diagrams under different dynamic parameters

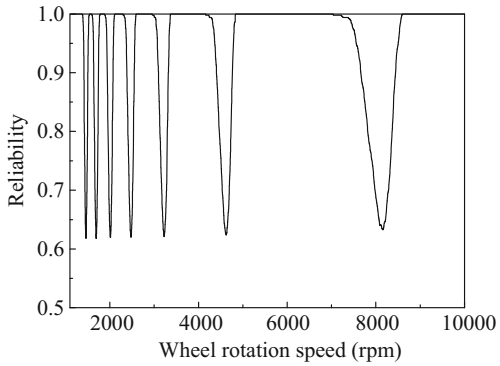

Fig. 6 Relationship between the reliability and the wheel rotation speed

the grinding dynamic parameters. Monte Carlo method is used to calculate structural reliability, and the limit state equation can be expressed as:

$$U(\mathbf{X}) = K_{\mathrm{n}} - K_{\mathrm{n0}} \tag{20}$$

If $U(\mathbf{X}) > 0$ in the calculations of sampling by N times, the actual contact stiffness is larger than the theoretical calculation result, and the chatter is more powerful than before. This phenomenon may result in a negative effect on the workpiece's surface. It is assumed that the calculation time is set as $N = 5000$. If $U(\mathbf{X}) < 0$ in the calculations of sampling by N times, it is of little effect in the generation of workpiece's topography. On the assumption that among the N times sampling there are S times samplings making $U(\mathbf{X}) < 0$, the reliability of the system can be written as:

$$P = \frac{S}{N} \tag{21}$$

Where K_{n0} is the given contact stiffness without considering the uncertainty. $\mathbf{X}$ is a defined variable matrix. $\mathbf{X} = (M_{\mathrm{g}}, C_{\mathrm{g}}, K_{\mathrm{g}}, \omega)^{\mathrm{T}}$. M_{g}, K_{g}, and C_{g} are linearly independent with each other, but they all linearly depend on the chatter frequency ω. According to Eq. (19), ω is decided by M_{g}, K_{g}, C_{g}, and the wheel rotation speed N_{g}. As a consequence, N_{g} can indirectly change the chatter state by influencing the chatter frequency ω. Figure 6 shows the relationship between the grinding chatter's reliability and the wheel rotation speed. It can be seen that the system's reliability are not the same all the time. With the increase of the spindle's speed, the change of reliability decreases.

The chatter frequency ω depends on M_{g}, K_{g}, C_{g}, and N_{g} of the system. Therefore, $\mathbf{X}$ turns into a matrix with relevant variables. In order to obtain the distribution of $\mathbf{X}$, the distribution of ω should be studied. In addition, due to the machining errors, multiple random selection is carried out on M_{g}, K_{g}, C_{g}, and N_{g}. Therefore, the value of ω is confirmed. Figure 7 shows the relationship between chatter frequency and wheel rotation speed under different machining errors.

After the chatter frequency is obtained, measures should be taken to calculate the system's reliability. Orthogonal transformation method is applied to transform the relevant variables into independent random variables. As a result, the correlation matrix which is composed of M_{g}, K_{g}, C_{g}, and ω can be written as:

$$\boldsymbol{\rho} = \begin{pmatrix} 1 & 0 & 0 & \rho_{M_{\mathrm{g}}\omega} \\ 0 & 1 & 0 & \rho_{C_{\mathrm{g}}\omega} \\ 0 & 0 & 1 & \rho_{K_{\mathrm{g}}\omega} \\ \rho_{M_{\mathrm{g}}\omega} & \rho_{C_{\mathrm{g}}\omega} & \rho_{K_{\mathrm{g}}\omega} & 1 \end{pmatrix} \tag{22}$$

Where $\rho_{M_{\mathrm{g}}\omega}$, $\rho_{C_{\mathrm{g}}\omega}$, and $\rho_{K_{\mathrm{g}}\omega}$ are the correlation coefficient of M_{g}, K_{g}, and C_{g} with ω respectively. Therefore, the covariance matrix can be written as:

$$\mathbf{C} = \begin{pmatrix} \sigma^2_{M_{\mathrm{g}}} & 0 & 0 & \rho_{M_{\mathrm{g}}\omega}\sigma_{M_{\mathrm{g}}}\sigma_{\omega} \\ 0 & \sigma^2_{C_{\mathrm{g}}} & 0 & \rho_{C_{\mathrm{g}}\omega}\sigma_{C_{\mathrm{g}}}\sigma_{\omega} \\ 0 & 0 & \sigma^2_{K_{\mathrm{g}}} & \rho_{K_{\mathrm{g}}\omega}\sigma_{K_{\mathrm{g}}}\sigma_{\omega} \\ \rho_{M_{\mathrm{g}}\omega}\sigma_{M_{\mathrm{g}}}\sigma_{\omega} & \rho_{C_{\mathrm{g}}\omega}\sigma_{C_{\mathrm{g}}}\sigma_{\omega} & \rho_{K_{\mathrm{g}}\omega}\sigma_{K_{\mathrm{g}}}\sigma_{\omega} & \sigma^2_{\omega} \end{pmatrix} \tag{23}$$

Where $\sigma^2_{M_{\mathrm{g}}}$, $\sigma^2_{C_{\mathrm{g}}}$, $\sigma^2_{K_{\mathrm{g}}}$, and σ^2_{ω} are the variance of the M_{g}, K_{g}, C_{g}, and ω respectively. Due to the property of fourth-order symmetric positive matrix, there must be four characteristics and four linearly independent characteristic vectors. $\mathbf{Y}$ is the new matrix after the orthogonal transformation, and $\mathbf{A}$ is the matrix made up of four regularization characteristic vectors.

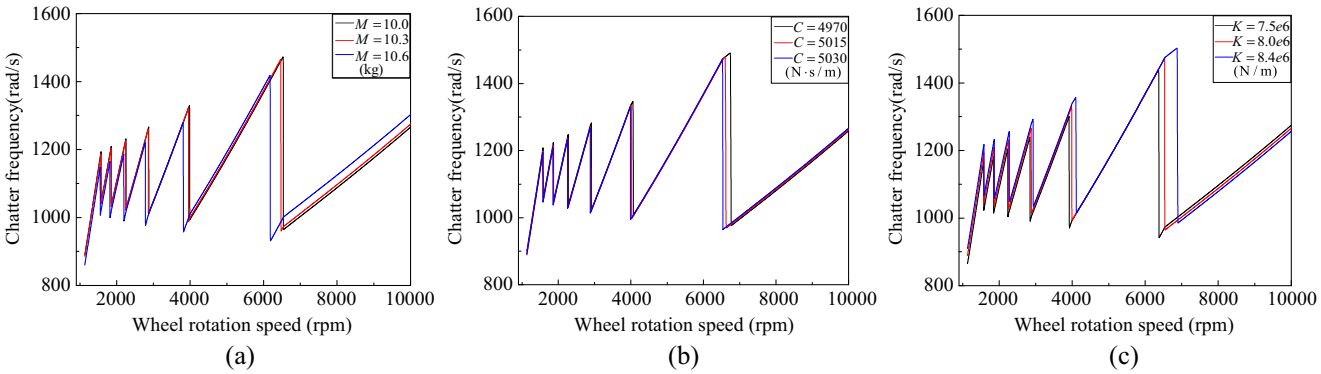

Fig. 7 Relationship between the reliability and the wheel rotation speed

$$\mathbf{Y} = A^{\mathrm{T}}\mathbf{X} \tag{24}$$

$$\mu\mathbf{Y} = A^{\mathrm{T}}\mu\mathbf{X} \tag{25}$$

$$\sigma\mathbf{Y} = A^{\mathrm{T}}\mathbf{C}\mathbf{A} \tag{26}$$

For the reason that $\mathbf{Y}$ is an independent matrix, Monte Carlo method is applied to calculate the system's reliability. In order to verify the accuracy of the results with FOSM method, $U(\mathbf{X})$ can be written as:

$$W = U(\mathbf{X}) = U(\mathbf{A}\mathbf{Y}) = U_{\mathrm{Y}}(\mathbf{Y}) \tag{27}$$

The derivative of $\mathbf{Y}$ can be obtained with the check-point method, and Eq. (27) can be transformed into:

$$\frac{\partial U_{\mathrm{Y}}(\mathbf{Y})}{\partial Y_{\mathrm{i}}} = \mathbf{A}^{T}\frac{\partial U(\mathbf{X})}{\partial X_{\mathrm{i}}} \tag{28}$$

According to the linear combination of independent random variables, the mean and the standard deviation of the U_Y can be written as:

$$\mu U_{\mathrm{Y}} = g(\mathbf{Y}) + \sum_{i=1}^{4}\frac{\partial g(\mathbf{Y})}{\partial Y_{\mathrm{i}}}\left(\mu_{\mathrm{Y_i}} - Y_{\mathrm{i}}\right) \tag{29}$$

$$\sigma U_{\mathrm{Y}} = \sqrt{\sum_{i=1}^{4}\left(\frac{\partial g(\mathbf{Y})}{\partial Y_{\mathrm{i}}}\right)^{2}\sigma_{\mathrm{Y_i}}^{2}} \tag{30}$$

As a result, the reliability index can be obtained:

$$\beta = \frac{\mu U_{\mathrm{Y}}}{\sigma U_{\mathrm{Y}}} \tag{31}$$

The sensitivity coefficient of $\mathbf{Y}$ can be written as:

$$\cos\theta_{Y_{\mathrm{i}}} = -\frac{\frac{\partial g(\mathbf{Y})}{\partial Y_{\mathrm{i}}}\sigma_{Y_{\mathrm{i}}}}{\sqrt{\sum_{i=1}^{4}\left(\frac{\partial g(\mathbf{Y})}{\partial Y_{\mathrm{i}}}\right)^{2}\sigma_{Y_{\mathrm{i}}}}} \tag{32}$$

Therefore, the new $\mathbf{Y}$ can be written as

$$\mathbf{Y} = \mu_{Y_{\mathrm{i}}} + \beta\sigma_{Y_{\mathrm{i}}}\cos\theta_{Y_{\mathrm{i}}} \tag{33}$$

Then $\mathbf{X}$ is updated by $\mathbf{X} = \mathbf{A}\mathbf{Y}$. Multiple iterations does not come to an end until the error is less than 10^{-3}. Finally, the results about the reliability of grinding system and the given contact stiffness K_{n0} with two methods are shown in Fig. 8.

As is shown in Fig. 8, the red line represents the reliability results which are calculated with MC method, and the black line represents the reliability results which are calculated with FOSM method. For the reason that the results show consistency, the accuracy of the methods is verified. It can be seen that the reliability of the grinding system decreases when the given contact stiffness becomes higher due to the increase of the chatter's amplitude (shown in Fig. 4). As a result, serious vibration of the grinding system is caused. As more and more K_{n} exceed K_{n0} in the multiple sampling calculations, the reliability of the grinding system decreases when the contact stiffness increases.

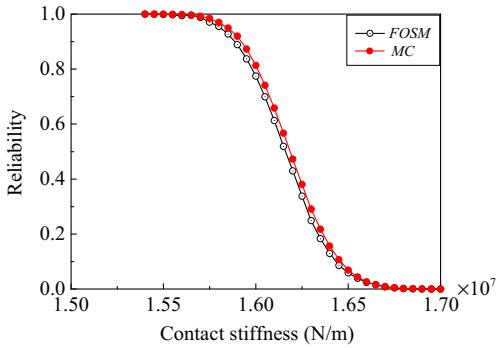

Fig. 8 Reliability with the contact stiffness at the wheel rotation speed of 2828 rpm

Figure 9 shows the change of the reliability when the given contact stiffness K_{n0} and the wheel's wheel rotation speed N_{g} are taken into consideration. It can be seen that under different wheel rotation speeds, the reliability of the system reduce with the increase of the contact stiffness. However, the attenuation rates are different. With the decrease of the wheel rotation speed, the attenuation rates become higher. The accuracy of the workpiece cannot be guaranteed if the reality of the grinding system becomes too low. Therefore, the workpiece benefits from the appropriate increase of the wheel rotation speed.

4 Modeling of the wheel surface topography

The machining efficiency and the workpiece surface topography depend on the distribution of the wheel's grains to a big extent. However, it is rather time-consuming to obtain the data

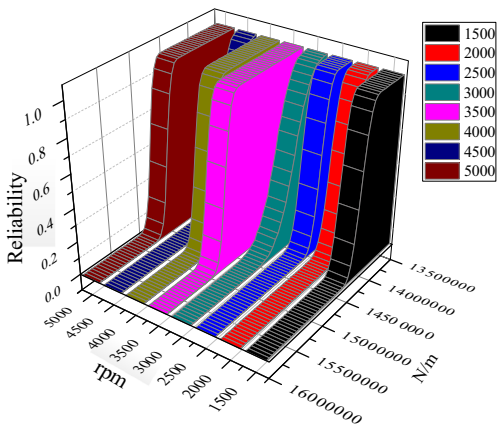

Fig. 9 Reliability with the contact stiffness at different wheel rotation speeds

of the wheel's surface topography. Therefore, it really becomes a necessary step to establish the grains distribution on the wheel's surface for the whole simulation procedure. For the reason that the peak of the rough surface is easier to be removed than the valley in the machining process, the wheel's surface shows negative skewness. Therefore, the digit generation technology which is based on the linear filtering technology and the Johnson Transformation are proposed to simulate the wheel's surface topography.

The wheel's surface can be regarded as a two-dimension spatial random surface, and the grains' sizes on the surface can be discretized by changing the height of $z(i,j)$. $z(i,j)$ is described by the autocorrelation function and the first four center moments (expectation $\overline{u}$, variance σ^2, skewness sk, kurtosis ku). It can be seen that $z(i,j)$ belongs to the non-Gaussian distribution and can be calculated by the Johnson transformation. The Johnson transformation is classified into four kinds of systems:

a. Unbounded system

$$z' = \gamma + \delta \sinh^{-1}\left(\frac{z-\xi}{\lambda}\right) \tag{34}$$

b. Bounded system

$$z' = \gamma + \delta \log\left(\frac{z-\xi}{\xi+\lambda-z'}\right) \tag{35}$$

c. Logarithmic system

$$z' = \gamma + \delta \log\left(\frac{z-\xi}{\lambda}\right) \tag{36}$$

d. Normal system

$$z' = \gamma + \delta z \tag{37}$$

Where z' is the Gaussian distribution, while z is the non-Gaussian distribution γ, δ, ξ, and λ are calculated with the Hill method [26]. The parameters are according to the results of the input skewness and kurtosis.

$$sk_\eta = \frac{\left(\sum_{r=1}^{M}\sum_{s=1}^{N} h(r,s)^2\right)^{3/2}}{\sum_{r=1}^{M}\sum_{s=1}^{N} h(r,s)^3} sk_z \tag{38}$$

$$k_\eta = \frac{\left(\sum_{r=1}^{M}\sum_{s=1}^{N} h(r,s)^2\right)^{2}}{\sum_{r=1}^{M}\sum_{s=1}^{N} h(r,s)^4} (k_z - 3) + 3 \tag{39}$$

Where sk_η and k_η are the input skewness and kurtosis respectively. sk_z and k_z are the output skewness and kurtosis respectively.

As the wheel's surface has the particular autocorrelation characteristic, it becomes necessary to carry out a two-dimension linear filtering on the non-Gaussian distribution. Therefore, z can be written as:

$$z(i,j) = \sum_{r=1}^{M}\sum_{s=1}^{N} h(r,s)\overline{z}(i+r, j+s) \tag{40}$$

Where h is the filter function of the wheel surface. $\overline{z}$ is the non-Gaussian distribution which is obtained via Johnson transformation. Fourier transformation is applied to Eq. (38):

$$Z(k,l) = H(k,l)\overline{Z}(k,l) \tag{41}$$

Where Z, H, and $\overline{Z}$ are the Fourier transformation of z, h, and $\overline{z}$. Therefore, $H(k,l)$ can be written as:

$$H(k,l) = \sum_{r=1}^{M}\sum_{s=1}^{N} h(r,s)e^{-(jkr+jls)} \tag{42}$$

Since the power spectral density can be expressed into the square modulus of the Fourier transformation, Eq. (41) can be written as:

$$S_z(k,l) = |H(k,l)|^2 S_{\overline{z}}(k,l) \tag{43}$$

Where $S_z(k,l)$ and $S_{\overline{z}}(k,l)$ are the power spectral density functions of the output and input sequence respectively. The power spectral density function can also be obtained from the Fourier Transformation of autocorrelation function. Therefore, $S_z(k,l)$ can also be written as:

$$S_z(k,l) = \frac{1}{MN}\sum_{r=1}^{M}\sum_{s=1}^{N} R(k,l)\exp\left(-\frac{2\pi kr}{M} - \frac{2\pi ls}{N}\right) \tag{44}$$

Where $R(k,l)$ can be written as

$$R(k,l) = \sigma^2 \exp\left\{-2.3\left[\left(\frac{k}{\beta_x}\right)^2 + \left(\frac{l}{\beta_y}\right)^2\right]^{1/2}\right\} \tag{45}$$

Where β_x and β_y are the autocorrelation lengths in the direction of x and y respectively. The autocorrelation lengths are defined as the lengths in x and y directions where the exponential drops to 10% from its original value. Based on the distribution of the abrasive grains, the simulation model is chosen as isotropic and β_x is equivalent with β_y. As a result, the exponential autocorrelation function can be only considered in one direction instead of both two directions. The autocorrelation of the simulation surface is calculated and compared with R_x. Figure 10 shows the result of R in x direction. The black line is obtained from the theoretical calculation, while the red one is calculated from the non-Gaussian simulation in x direction (Fig. 11).

5 Modeling of the workpiece's topography with grinding chatter

5.1 Modeling of workpiece's surface

The workpiece's surface topography is decided by the chatter of the grinding system and the interference between the grains and the workpiece. The former factor has been analyzed in the paragraph above. The latter factor has been analyzed through establishing the grains dynamic model. Then the chatter factor is coupled with the dynamic model. For the reason that grinding is a complex material removal process, several hypotheses are adopted as follows before the grains dynamic model is established:

1. Sliding, plowing, and built-up edges are not taken into consideration in the process of grinding.
2. Thermal deformation is not associated with the grains dynamic model.

Figure 12 shows the trajectory of the adjacent grains as the grinding is processing. The origin of coordinate of the systems is set on the workpiece's surface, on which the lowest grain of the wheel contacts with the workpiece. The grinding way is

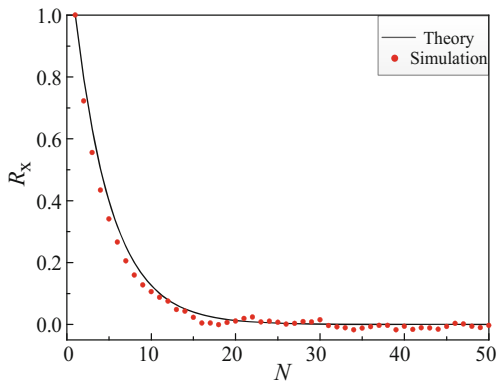

Fig. 10 The autocorrelation function with two methods

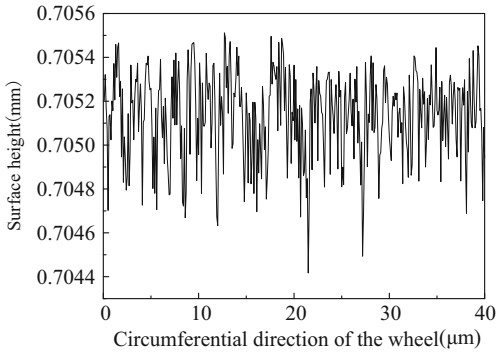

Fig. 11 The non-Gaussian distribution

up-grinding. The dynamic equations of grain G can be written as:

$$\begin{cases} x = v_w t + r_s \sin\theta \\ y = r_s(1-\cos\theta) \end{cases} \tag{46}$$

Where x and y are the instantaneous coordinates in x and y direction respectively. θ is the rotation angle of the wheel. r_s is the generalized radius of the wheel. t is the time needed to rotate the grain at the angle of θ. When t is eliminated, Eq. (46) can be written as:

$$y = \frac{x^2}{2r_s\left(1+\frac{v_w}{v_s}\right)^2} \tag{47}$$

When the grain size is taken into consideration, the trajectory of each grain in the local coordinate system can be written as:

$$y_j' = \frac{x_j'^2}{2r_j\left(1+\frac{v_w}{v_s}\right)^2} \tag{48}$$

Where x_j' and y_j' are the local coordinates of the jth grain in the local coordinate system. r_j is the actual radius which can be written as $r_j = h_j + r_s$. Where h_j is the non-Gaussian distribution of the wheel. In order to obtain h_j, the original input expectation and standard deviation of the grain can be written as:

$$d_g = 68M^{-1.4} \tag{49}$$

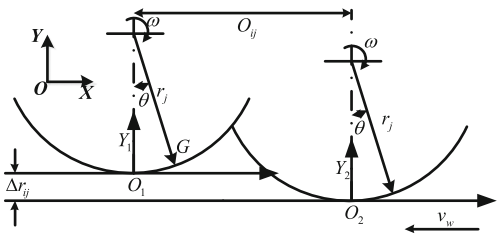

Fig. 12 Trajectory of the adjacent grains

$$\sigma_g = \left(15.2M^{-1} - 68M^{-1.4}\right)\Big/3 \tag{50}$$

Where M is the abrasive granularity of the wheel.

For the adjacent grains, the interval between the translation and the rotation are equal. In order to know the trajectory of each grain, the local coordinate system is transformed into the global coordinate system. Meantime, the dynamic solution of the grinding system is coupled with the grain dynamic equation by obtaining the permeation of the workpiece and the wheel. Therefore, the equation about each grain including the grinding chatter in the global coordinate system can be written as:

$$y_j = \frac{\left(x - \Delta O_j\right)^2}{2r_j\left(1 + \frac{v_w}{v_s}\right)^2} - \left(r_j - r_1\right) + \varepsilon_g(t) + \varepsilon_w(t) \tag{51}$$

Where ΔO_j is the wheel's translation distance when the jth grain is passed to the origin of the corresponding local coordinate system, which can be written as:

$$\Delta O_j = \frac{v_w}{v_s}(n-1)\Delta x_s \tag{52}$$

Where v_s is the linear velocity of the wheel. n is the grain number in the circumferential direction. Δx_s is the circumferential distance between the adjacent grains, which can be written as:

$$\Delta x_s = d_g \sqrt[3]{\frac{\pi}{12(32 - S)}} \tag{53}$$

$$n = \frac{2\pi r_s}{\Delta x_s} \tag{54}$$

Where S is the wheel's structure number. In order to combine the feasibility of the experimental parameters, wheel rotation speed is set as $N_g = 2828$ rpm, and the abrasive granularity of the wheel is set as $M = 46$, and the radius of the wheel is set as $r_s = 0.125$ m, and the velocity of the workpiece is set as $v_w = 0.03$ m/s, and the grinding depth is set as $a_p = 100$ μm.

Figure 13 shows the simulated 3D workpiece's topography under four different conditions, in which panel a has the given parameters, while panel b excludes the chatter factor, and panel c has $N_g = 4000$ rpm as the wheel rotation speed, and panel d has $v_w = 0.08$ m/s as the workpiece's feeding rate. It can be

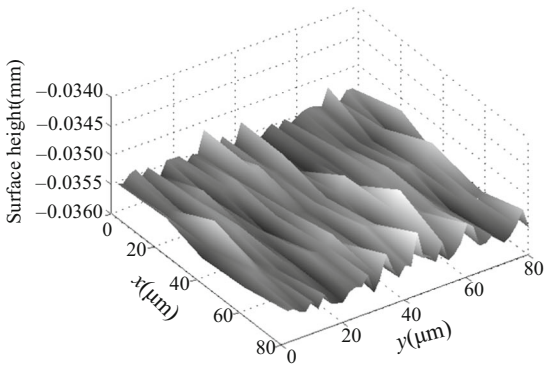

(a) with the given parameters

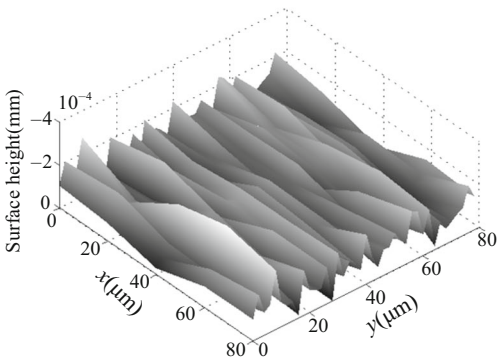

(b) without the chatter factor

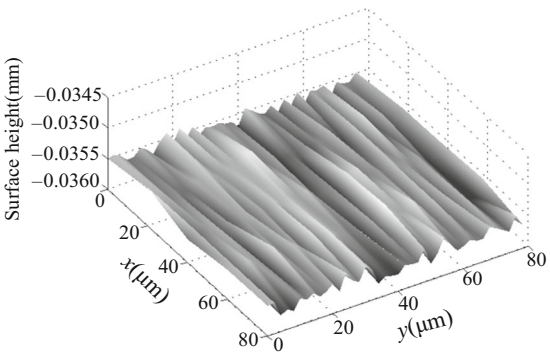

(c) with the rotation speed N_g = 4000 rpm

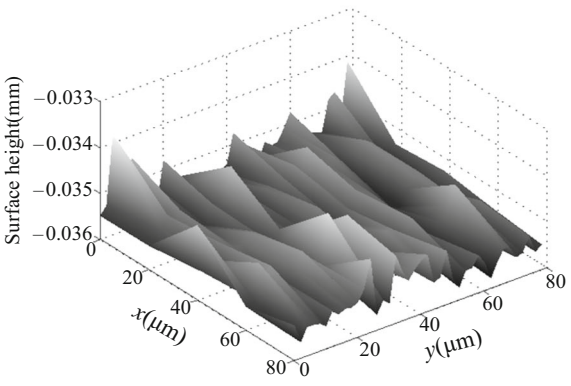

(d) with the feeding rate v_w = 0.08 m/s

Fig. 13 The 3D workpiece's topography under four different conditions

seen that the chatter factors have a great influence on the workpiece's topography, while the workpiece's topography has a close relationship with the wheel rotation speed and the feeding rate, and the specific relationship is shown in Fig. 14.

5.2 Analysis on workpiece's grinding parameters

Two different conditions are considered in Fig. 14. One is with the chatter factor, while the other is without the chatter factor. Figure 14a shows the relationship between the surface's height and the wheel rotation speed under different abrasive granularities. Figure 14b shows the relationship between the surface height and the feeding rate under different abrasive granularities. From Fig. 14, the following conclusions can be obtained:

1. The surface height decreases when the wheel rotation speed increases. Even though the contact stiffness of the grinding system fluctuates with the increase of the wheel rotation speed, the grinding depth of a single grain decreases. As the grinding depth becomes shallow, the elastic deformation is easier to recover. When the feeding rate increases, the grinding depth of a single grain increases. The increasing depth results in more serious interference, which leads to a poor surface topography.

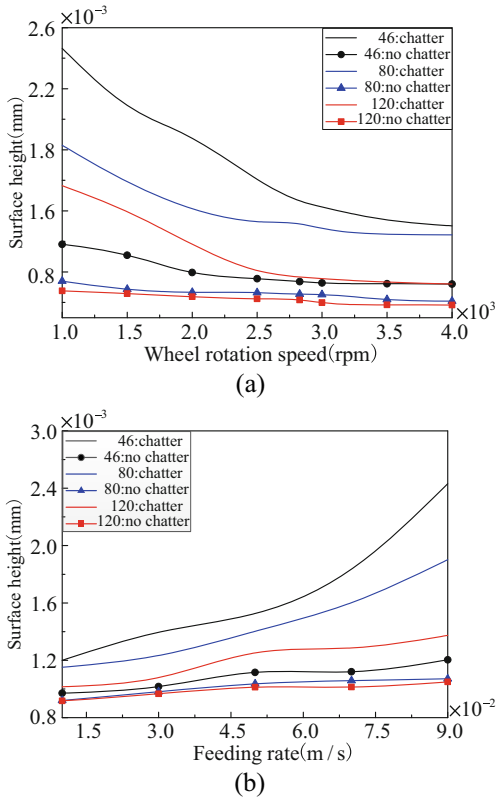

Fig. 14 The surface height at different wheel rotation speeds and feeding rates in two situations

2. The surface height decreases with the increase of the abrasive granularity. The reason is that the increasing abrasive granularity means the smaller size of the grain. The smaller size contributes to the smaller interference of each grain and results in a superior surface topography. Therefore, the relationship between the surface height and the abrasive granularity is shown in Fig. 14.

3. Through comparing the two conditions (with chatter factor and without chatter factor), it can be seen that chatter can lead to poor surface topography. The reason is that chatter can make the grinding system unstable, and make the workpiece's surface vibrate. As a result, the amplitude of the surface height becomes higher compared with the condition without the chatter factor.

5.3 Analysis on workpiece's dynamic parameters

After analyzing chatter's influence on the workpiece's topography, the relationship between the dynamic parameters and the workpiece's surface topography should be studied. Figure 15 shows the relationship between the surface height and the increasing wheel rotation speed under three different dynamic parameters (M_g, K_g, C_g).

It can be seen that the surface height increases with the increase of the C_g and K_g under some conditions, but it decreases with the increase of M_g, which coincides with the results of stability analysis. The contact stiffness between the wheel and the workpiece increases with the increase of the C_g and K_g, and the grinding force which is needed to generate unit displacement becomes bigger. The increasing grinding force leads to bigger plastic deformation on the workpiece's surface, which can result in poor surface topography due to the serious chatter. However, the contact stiffness reduces with the increase of M_g. Therefore, the grinding force becomes smaller and the crack caused by the grain becomes shallow. As a result, the surface height becomes superior compared with the first two conditions.

It is the machining errors that lead to the uncertainty of the grinding system, and the uncertainty is measured by the structure reliability. The contact stiffness is the key parameter to evaluate the reliability and the chatter strength of the grinding system. The reliability of the grinding system decreases with the increase of the contact stiffness, and the increasing contact stiffness also leads to more serious chatter. As a consequence, the dynamic impacts caused by the serious chatter acts on the workpiece directly. In this way, poor surface topography is generated with the increase of the contact stiffness, which is shown in Fig. 16.

According to the relationship between the surface height and the contact stiffness, it can be concluded that the low reliability which is caused by the increasing contact stiffness can result in more serious chatter and worse surface topography.

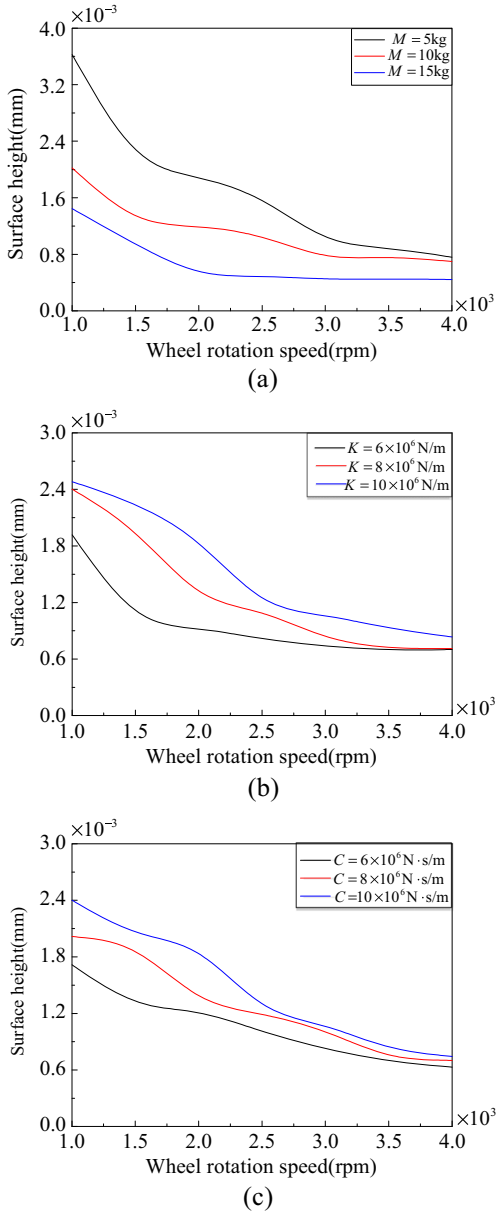

Fig. 15 Relationship between surface height and the increasing wheel rotation speed under different dynamic parameters

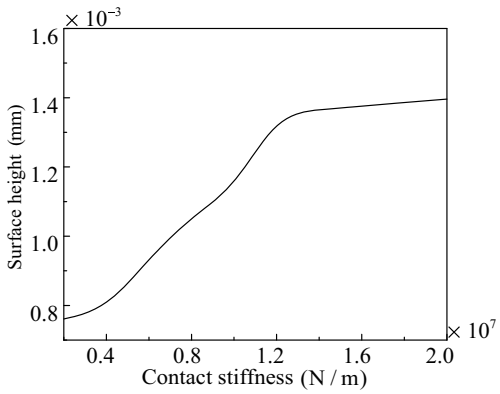

Fig. 16 Surface height under different contact stiffness

Table 1 Experimental conditions and parameters

Experimental conditions	Parameters
Experiment equipment	M7120A
Wheel rotation speed	2828 rpm
Grinding wheel	White corundum
Granularity of the wheel	F46
Diameter of the wheel	250 mm
Size of the workpiece	50 × 10 × 20 mm

6 Experimental investigation

6.1 Condition and process of the experiment

In order to study the workpiece's surface height with the grinding chatter taken into consideration, the experiment is conducted specially. Through comparing the chatter's simulation results with experimental results, the accuracy of the theoretical model is verified to be reasonable.

In the experiment, the type of the surface grinder is M7120A. The wheel rotation speed is 2828 rpm, the diameter of which is 250 mm. The vitrified bond white alumina wheel is chosen with the abrasive granularity F46. The material of the workpiece is steel 45 with the size of (50 × 10 × 20) mm. They are summarized in Table 1. The workpiece is fixed on the clamp at the feeding rate of 0.033 m/s. The grinding depth of the workpiece is 100 μm. The grinding process and experiment devices are shown in Fig. 17.

By using diamond stylus at the curvature radius of 2.5–10 mm, the workpiece surface height is obtained with contact interference method. The TR300 surface measuring instrument is used in this experiment. The working principle and the measuring devices are shown in Fig. 18.

Experiments are carried out at different workpiece's feeding rates, 0.013, 0.022, and 0.033 m/s respectively, while the other parameters stay the same. Afterwards, comparison of the surface heights is done among the experimental results, the simulation results (with the chatter factor), and the simulation results (without chatter factor).

Since the chatter strength varies with the different positions on the workpiece, the workpiece's surface is

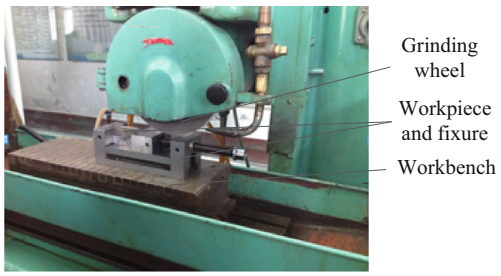

Fig. 17 The grinding process and the experiment devices

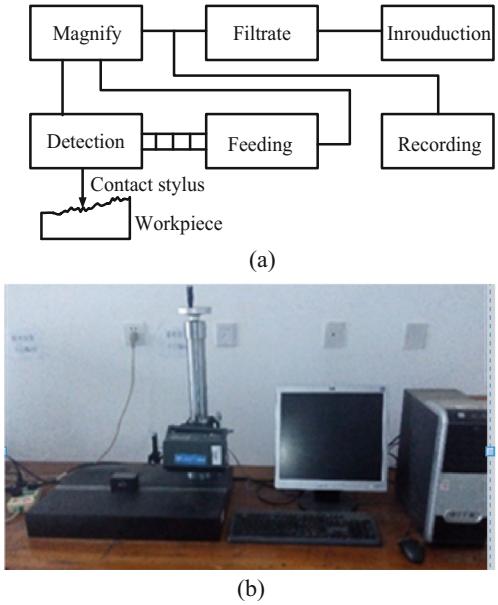

Fig. 18 The working principle and the measuring devices

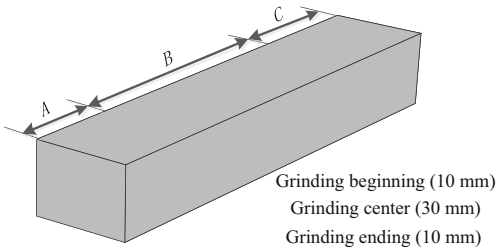

Fig. 19 The grinding sections on the workpiece

divided into three sections for analysis, the grinding beginning area, the grinding center area, and the grinding ending area, which is shown in Fig. 19. The surface heights of these three sections are recorded respectively. Afterwards, the comparison is carried out between the simulation results and the experimental results of the three sections.

Table 2 Experimental surface height at different feeding rates and different sections on the workpiece

v_w (m/s)	A (μm)	B (μm)	C (μm)
0.013	1.085	1.504	1.505
	1.316	1.541	1.463
	1.415	1.439	1.677
0.022	1.341	1.572	1.651
	1.182	1.420	1.616
	1.303	1.681	1.430
0.033	1.103	1.473	1.882
	1.340	1.523	1.545
	1.227	1.521	1.758

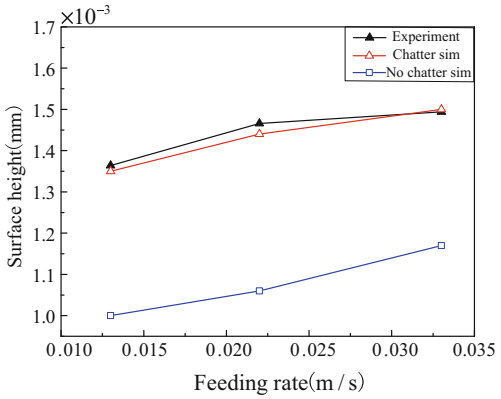

Fig. 20 Predicted and measured surface height at different feeding rates

6.2 Analysis on the experiment results

The mean-values of the surface heights from multiple measurements are summarized in Table 2. The relationship between the surface height and the workpiece's feeding rate is shown in Fig. 20. Through the comparison of the surface height between the experiment results and the simulation results, it can be seen that the experiment results match the simulation result with chatter factor well. Both of their surface heights increase with the increase of the workpiece's feeding rate. However, when the chatter factor is not considered, the preciseness of the simulation results cannot be guaranteed. For the reason that the chatter makes the grinding system unstable, it should be considered in the analysis of workpiece's topography.

When the workpiece's feeding rate stays at 0.033 m/s, the relationship between the surface heights and the different sections on the workpiece is shown in Fig. 21. In spite of the serious chatter of grinding system at the beginning of the grinding, the grinding depth is relatively small, and this small depth plays the dominant role compared with the grinding chatter. Due to the increasing grinding depth and the grinding chatter, the surface height increases with the increase of the feeding distance. When the grinding process is nearly to the

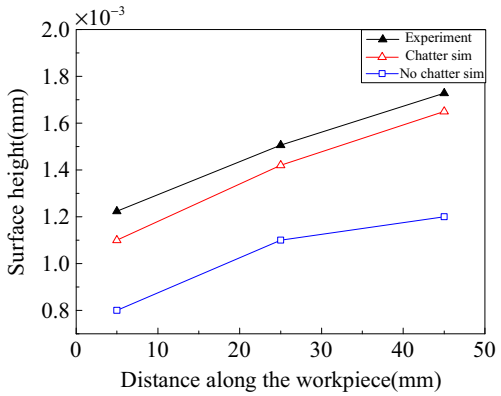

Fig. 21 Surface height on the different workpiece's sections

end, the edge effect and the grinding chatter play the dominant role in deciding the workpiece's surface topography.

7 Conclusions

In this paper, a new model combined the grains of non-Gaussian distribution with the grinding chatter is established to study the relationship between the dynamic characteristic and the workpiece's surface topography.

The results of the above dynamic analysis show that the chatter strength is influenced by the contact stiffness between the wheel and the workpiece. The low reliability caused by the contact stiffness can lead to poor surface topography. The surface height and the contact stiffness decrease with the increase of M_g. However, a reverse tendency is shown when K_g and C_g increase.

The grinding parameters composed of wheel rotation speed, the feeding rate, and the abrasive granularity directly influence the surface height. The surface height reduces with the increase of the wheel rotation speed and the abrasive granularity. However, it increases with the increase of the feeding rate.

The simulation is further validated by the experiment at different feeding rates and sections on the workpiece. It shows that the grinding chatter can raise the workpiece's surface height by affecting the grinding system. Grinding chatter is a key factor to influence the workpiece surface topography and it cannot be neglected in the practical surface grinding compared with the cylindrical grinding.

Acknowledgements This project is supported by the National Natural Science Foundation of China (Grant No. 51375083) and the Technology Project of Shenyang City (Grant No. F16-205-1-02).

References

1. Cao Y, Guan J, Li B, Chen X, Yang J, Gan C (2013) Modeling and simulation of grinding surface topography considering wheel vibration. Int J Adv Manuf Technol 66(5):937–945
2. Koshy P, Ives LK, Jahanmir S (1999) Simulation of diamond-ground surfaces. Int J Mach Tools Manuf 39(9):1451–1470
3. Zhang D, Li C, Jia D, Zhang Y, Zhang X (2015) Specific grinding energy and surface roughness of nanoparticle jet minimum quantity lubrication in grinding. Chin J Aeronaut 28(2):570–581
4. Doman DA, Warkentin A, Bauer R (2006) A survey of recent grinding wheel topography models. Int J Mach Tools Manuf 46(3–4):343–352
5. Jia D, Li C, Zhang Y, Zhang D, Zhang X (2016) Experimental research on the influence of the jet parameters of minimum quantity lubrication on the lubricating property of Ni-based alloy grinding. Int J Adv Manuf Technol 82(1):617–630
6. Deng Y, Xiu S, Shi X, Sun C, Wang Y (2017) Study on the effect mechanisms of pre-stress on residual stress and surface roughness in PSHG. Int J Adv Manuf Technol 88(9):3243–3256
7. Wang X, Yu T, Dai Y, Shi Y, Wang W (2016) Kinematics modeling and simulating of grinding surface topography considering machining parameters and vibration characteristics. Int J Adv Manuf Technol 87(9):2459–2470
8. Zhang N, Kirpitchenko I, Liu DK (2005) Dynamic model of the grinding process. J Sound Vib 280(1–2):425–432
9. Wang Y, Moon KS (1997) A methodology for the multi-resolution simulation of grinding wheel surface. Wear 211(2):218–225
10. Liu Y, T-x L, Liu K, Y-m Z (2016) Chatter reliability prediction of turning process system with uncertainties. Mech Syst Signal Process 66–67:232–247
11. Yan Y, Xu J, Wiercigroch M (2014) Chatter in a transverse grinding process. J Sound Vib 333(3):937–953
12. Chung K-w, Liu Z (2011) Nonlinear analysis of chatter vibration in a cylindrical transverse grinding process with two time delays using a nonlinear time transformation method. Nonlinear Dyn 66
13. Tobias S (1965) Machine Tool Vibration Blackie. London
14. Altintas Y, Budak E (1995) Analytical prediction of stability lobes in milling. CIRP Annals-Manufacturing Technology 44(1):357–362
15. Duncan GS, Kurdi, Schmitz TL, Snyder JP Uncertainty propagation for selected analytical milling stability limit analyses. In: North American manufacturing research conference, 2006. pp 17–24
16. Graham E, Mehrpouya M, Park SS (2013) Robust prediction of chatter stability in milling based on the analytical chatter stability. J Manuf Process 15(4):508–517
17. Zhang M (2009) Structural reliability analysis method and procedures. Beijing, China
18. Xu L, Cheng G (2003) Discussion on: moment methods for structural reliability. Struct Saf 25(2):193–199
19. Zhou X, Xi F (2002) Modeling and predicting surface roughness of the grinding process. Int J Mach Tools Manuf 42(8):969–977
20. Yan L, Rong Y, Jiang F (2011) Quantitive evaluation and modeling of alumina grinding wheel surface topography. Jixie Gongcheng Xuebao (Chinese Journal of Mechanical Engineering) 47(17):179–186
21. Xie Y, Williams JA (1996) The prediction of friction and wear when a soft surface slides against a harder rough surface. Wear 196(1):21–34
22. Qiao G, Dong G, Zhou M (2013) Simulation and assessment of diamond mill grinding wheel topography. Int J Adv Manuf Technol 68(9):2085–2093
23. Nguyen TA, Butler DL (2005) Simulation of precision grinding process, part 1: generation of the grinding wheel surface. Int J Mach Tools Manuf 45(11):1321–1328
24. Yang X, Guo Y (2005) Study on the micro-vibration test system in ultra precision aspheric surface grinding. J Fuzhou Univ (Natur Sci) 33(4):491–495
25. Yuan L, Keskinen E, Järvenpää V Stability analysis of roll grinding system with double time delay effects. In: IUTAM Symposium on Vibration Control of Nonlinear Mechanisms and Structures, 2005. Springer, pp 375–387
26. Hill I, Hill R, Holder R (1976) Algorithm AS 99: fitting Johnson curves by moments. J R Stat Soc: Ser C: Appl Stat 25(2):180–189